

# Fermi-Level-Dependent Charge-to-Spin Conversion of the Two-Dimensional Electron Gas at the $\gamma$ -Al<sub>2</sub>O<sub>3</sub>/KTaO<sub>3</sub> Interface

Hui Zhang<sup>1,\*</sup>, Zengtai Zhu,<sup>2</sup> Yungu Zhu,<sup>1</sup> Xiaobing Chen,<sup>3,4,5</sup> Qisheng Jiang,<sup>2</sup> Jinwu Wei,<sup>6</sup> Chenbo Zhao,<sup>7,8</sup> Jine Zhang,<sup>1</sup> Furong Han,<sup>1</sup> Huaiwen Yang,<sup>1</sup> Dapeng Zhu,<sup>1</sup> Hao Wu,<sup>2</sup> Yuansha Chen<sup>3,4</sup>, Fengxia Hu,<sup>2,3,4</sup> Baogen Shen,<sup>2,3,4</sup> Weisheng Zhao,<sup>1</sup> Jing Zhang,<sup>2,†</sup> Guoqiang Yu,<sup>2,3,9,‡</sup> and Jirong Sun<sup>2,3,4,10,§</sup>

<sup>1</sup>*School of Integrated Circuit Science and Engineering, Beihang University, Beijing 100191, China*

<sup>2</sup>*Songshan Lake Materials Laboratory, Dongguan, Guangdong 523808, China*

<sup>3</sup>*Beijing National Laboratory for Condensed Matter Physics, Institute of Physics, Chinese Academy of Sciences, Beijing 100190, China*

<sup>4</sup>*School of Physical Sciences, University of Chinese Academy of Sciences, Beijing 100049, China*

<sup>5</sup>*Shenzhen Institute for Quantum Science and Engineering (SIQSE) and Department of Physics, Southern University of Science and Technology, Shenzhen 518055, China*


<sup>6</sup>*Key Laboratory for Magnetism and Magnetic Materials of the Ministry of Education, Lanzhou University, Lanzhou 730000, China*

<sup>7</sup>*School of Science and Engineering, The Chinese University of Hong Kong, Shenzhen, Guangdong 518172, China*

<sup>8</sup>*Department of Chemical Physics, University of Science and Technology of China, Hefei, Anhui 230026, China*

<sup>9</sup>*Center of Materials Science and Optoelectronics Engineering, University of Chinese Academy of Sciences, Beijing 100049, China*

<sup>10</sup>*Spintronics Institute, Jinan University, Jinan 250022, Shandong Province, China*

 (Received 17 August 2022; revised 6 December 2022; accepted 10 February 2023; published 14 March 2023)

Charge-to-spin conversion is crucial for the application of emerging spintronic devices. A two-dimensional electron gas (2DEG) at a complex oxide interface usually possesses strong Rashba spin-orbit coupling, and spin-momentum locking offers a great possibility for efficient charge-to-spin conversion through the Rashba-Edelstein effect. Here, we report the fabrication of metallic 2DEGs in  $\gamma$ -Al<sub>2</sub>O<sub>3</sub>/KTaO<sub>3</sub> spinel/perovskite heterostructures and investigate the charge-to-spin conversion for Py/ $\gamma$ -Al<sub>2</sub>O<sub>3</sub>/KTaO<sub>3</sub> devices using the technique of spin-torque ferromagnetic resonance. The sizable spin splitting of the band structure results in a large current-induced spin-orbit torque efficiency with values up to around 3.6 at 5 K and about 1.1 at 300 K, which are more than an order of magnitude higher than those of heavy metals (0.07 for Pt at 300 K). Moreover, both theoretical and experimental results show that the charge-to-spin conversion is strongly dependent on the position of the Fermi level. These results demonstrate that optimizing the band filling of a KTaO<sub>3</sub>-based 2DEG is crucial for maximizing the conversion efficiency.

DOI: [10.1103/PhysRevApplied.19.034045](https://doi.org/10.1103/PhysRevApplied.19.034045)

## I. INTRODUCTION

Owing to Rashba spin-orbit coupling (SOC), the two-dimensional electron gas (2DEG) at the LaAlO<sub>3</sub>/SrTiO<sub>3</sub> (LAO/STO) interface has the characteristic of spin-momentum locking, i.e., both electron momentum and electron spin are constrained to the conductive interface and are locked orthogonally [1–3]. In this case, an electric current flowing along the interface will generate a perpendicular spin current, resulting in a charge-to-spin

conversion [4]. When this spin current is injected into a ferromagnetic layer, the effect of spin-orbit torque (SOT) will be produced, resulting in an electric switching of magnetization [5–7].

Based on SOT, the technique of spin-torque ferromagnetic resonance (ST-FMR) has been developed [8–11], making it possible to get a quantitative description of the efficiency of charge-to-spin conversion. Via ST-FMR, for example, a conversion efficiency of around 6 has been obtained for the LAO/STO 2DEG at room temperature [9]. This efficiency is more than an order of magnitude higher than those of heavy metals such as Pt, W, and Pd [5, 12, 13], etc. High conversion efficiency (about 4) is also found for LaTiO<sub>3+ $\delta$</sub> /STO 2DEG [10]. It seems to be a general property of the STO-based 2DEGs.

\*huizh@buaa.edu.cn

†zhangjing@sslabs.org.cn

‡guoqiangyu@iphy.ac.cn

§jrsun@iphy.ac.cn

As is well established, the efficiency of charge-to-spin conversion is governed by the Rashba SOC that emerges with the formation of the 2DEG in the interfacial layer of STO [3,9,14–16]. Notably, 2DEGs can also be formed at the interfacial layer of KTaO<sub>3</sub> (KTO), exhibiting similar transport behaviors to those of STO-based 2DEGs [17–20]. KTO is an oxide similar to STO in many aspects. However, KTO has a strong atomic SOC that is approximately 20 times as large as that of STO [21,22]. It is therefore reasonable to expect a strong Rashba SOC, thus an efficient charge-to-spin interconversion via KTO-based 2DEGs [23]. There are limited works on spin-to-charge conversion, the inverse process of charge-to-spin conversion, via the 2DEG at the interfacial layer of KTO. By thermally injecting spin current from the ferromagnetic EuO overlayer into the 2DEG at the EuO/KTO interface, Zhang *et al.* observed an electric output [24], i.e., spin current had been converted to charge current. Using the technique of spin pumping to inject spin current into Al/KTO 2DEG, Vicente-Arche *et al.* realized spin-to-charge conversion with an efficiency of  $\lambda_{\text{IEE}} \approx -3.5$  nm at 10 K [25]. Despite these works, many aspects of the KTO-based 2DEGs remain unexplored, for example, the process of charge-to-spin conversion. In this work, we perform a systematic investigation of charge-to-spin conversion via the 2DEG at the  $\gamma$ -Al<sub>2</sub>O<sub>3</sub>/KTO interface, based on the technique of ST-FMR at room temperature and low temperature. A conversion efficiency as high as approximately 3.6 at 5 K and 1.1 at 300 K are detected for the sample with a  $\gamma$ -Al<sub>2</sub>O<sub>3</sub> layer of 3 unit cell (u.c.), which are more than an order of magnitude higher than that of Pt (about 0.07 at 300 K). Moreover, a strong dependence of the conversion efficiency on band filling is observed, and the most efficient conversion takes place at the filling level corresponding to Lifshitz transition. Theoretical analysis indicates that enhanced spin splitting of the electronic band structure is responsible for efficient conversion.

## II. EXPERIMENT

### A. 2DEG preparation and characterization

High-quality 2DEGs are obtained by growing  $\gamma$ -Al<sub>2</sub>O<sub>3</sub> films on the (001)-oriented KTO single crystal substrate through pulsed laser deposition. Prior to film growth, we clean the substrate surface with alcohol and acetone successively, and there is no further surface treatment. The growth process is monitored by *in situ* reflection high-energy electron diffraction (RHEED). The target is a single crystal of  $\alpha$ -Al<sub>2</sub>O<sub>3</sub>. The fluence of the laser pulse is 2 J/cm<sup>2</sup> and the repetition rate is 2 Hz (KrF excimer laser, wavelength 248 nm). During the deposition process, the oxygen pressure is maintained at  $1 \times 10^{-4}$  Pa and the temperature of the substrate is kept at 700 °C. After deposition, the samples are cooled down to room temperature at a rate of 10 °C/min without changing the oxygen atmosphere.

The film thickness is determined by RHEED oscillations. The fabricated samples have the  $\gamma$ -Al<sub>2</sub>O<sub>3</sub> layers of 3, 4, 6, and 8 u.c., respectively. The surface morphology is investigated by atomic force microscopy (AFM, SPI 3800N, Seiko). The crystal structure of the films is determined by a Bruker x-ray diffractometer equipped with thin-film accessories (D8 Discover, Cu  $K\alpha$  radiation). The x-ray photoelectron spectroscopy (XPS) measurements are performed in a Thermo Scientific ESCALAB 250X instrument using a monochromatic Al  $K\alpha$  x-ray source. The electronic transport behavior of the  $\gamma$ -Al<sub>2</sub>O<sub>3</sub>/KTO heterostructures is measured by a Quantum-designed physical property measurement system employing van der Pauw geometry.

### B. ST-FMR device fabrication and measurement

The  $\gamma$ -Al<sub>2</sub>O<sub>3</sub>/KTO heterostructures are transferred into a chamber for magnetron sputtering, and then the chamber is evacuated up to the background pressure of  $1 \times 10^{-6}$  Pa. Permalloy (Py) films (6 nm) are deposited using magnetron sputtering at room temperature with an Ar pressure of 0.08 Pa. All samples are covered by Ta(3 nm)/MgO(2 nm) capping layers, where the MgO layer is used to protect the Py film from oxidation and the additional Ta layer is added to prevent moisture absorption by the MgO in air, which would lead to a deliquescence of the MgO layer. The Ta/MgO/Py/ $\gamma$ -Al<sub>2</sub>O<sub>3</sub>/KTO stacks are then patterned into rectangular strips of 20  $\mu$ m in width and 100  $\mu$ m in length by the standard photolithography and Ar-ion milling technique. The Au (80 nm)/Cr (5 nm) bilayers are deposited by magnetron sputtering as electrical contact pads. In the ST-FMR measurements, the radio-frequency current ( $I_{\text{rf}}$ ) with a nominal maximum power of 15 dBm is applied along the longitudinal direction of the rectangular bars ( $x$  axis). The in-plane external magnetic field ( $H$ ) with an angle of  $\varphi$  with respect to  $I_{\text{rf}}$  is swept during measurement. The ST-FMR measurements are performed at room temperature and a low temperature of 5 K, respectively.

## III. RESULTS AND DISCUSSION

### A. Structural characteristics and transport behavior of $\gamma$ -Al<sub>2</sub>O<sub>3</sub>/KTO heterostructures

Al<sub>2</sub>O<sub>3</sub> ultrathin film is usually  $\gamma$ -Al<sub>2</sub>O<sub>3</sub> with a spinel-type structure, rather than the common  $\alpha$ -Al<sub>2</sub>O<sub>3</sub> with a corundum structure; the surface energy differences thermodynamically stabilize  $\gamma$ -Al<sub>2</sub>O<sub>3</sub> over  $\alpha$ -Al<sub>2</sub>O<sub>3</sub> [26,27]. A schematic depiction of heteroepitaxial growth of the  $\gamma$ -Al<sub>2</sub>O<sub>3</sub> layer on the (001)-oriented KTO substrate is shown in Fig. 1(a). Despite differences in the cation sublattices, the oxygen sublattice of the spinel  $\gamma$ -Al<sub>2</sub>O<sub>3</sub> well matches that of the perovskite KTO. The lattice parameter of  $\gamma$ -Al<sub>2</sub>O<sub>3</sub> is 7.911 Å, which is nearly twice that of KTO ( $a_{\text{KTO}} = 3.989$  Å). The lattice mismatch is as small as

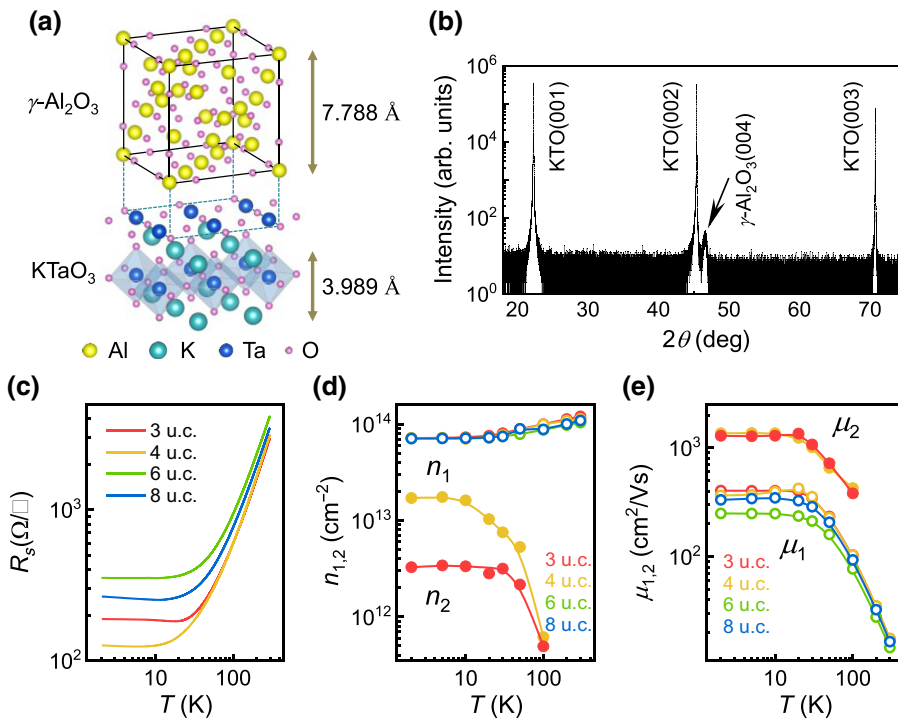


FIG. 1. (a) Sketch of the  $\gamma$ -Al<sub>2</sub>O<sub>3</sub>/KTO (001) heterostructure. (b) X-ray diffraction spectrum specifying the well-orientated  $\gamma$ -Al<sub>2</sub>O<sub>3</sub> film on KTO substrate. (c) Temperature dependence of the sheet resistance for samples with the  $\gamma$ -Al<sub>2</sub>O<sub>3</sub> thicknesses of 3, 4, 6, and 8 u.c. (d),(e) Corresponding carrier density and Hall mobility, respectively, as functions of temperature. Solid lines are guides to the eye.

0.84% [27]. Such an excellent lattice match between oxygen sublattices results in an epitaxial layer-by-layer growth of the  $\gamma$ -Al<sub>2</sub>O<sub>3</sub>/KTO spinel/perovskite heterostructures, as confirmed by the regular oscillations of the RHEED pattern (see Fig. S1 in the Supplemental Material [28]). As shown in Fig. 1(b), the x-ray diffraction (XRD) spectra further reveal the formation of a high-quality single crystalline  $\gamma$ -Al<sub>2</sub>O<sub>3</sub> film on the KTO substrate, and the out-of-plane lattice parameter is  $c = 7.788 \text{ \AA}$ , close to the bulk value  $7.911 \text{ \AA}$ . Here a  $\gamma$ -Al<sub>2</sub>O<sub>3</sub> film with a thickness of 16 nm is adopted for XRD measurements to get a clear signal. The obtained film is very flat, and the root-mean-squared roughness is around 0.21 nm (see Fig. S2 in the Supplemental Material [28]).

Al<sub>2</sub>O<sub>3</sub> is widely used as the best insulating material with a band gap normally above 8.0 eV. KTO is also a wide-band-gap insulator with a band gap of 3.6 eV. Fascinatingly, the interface between the two insulators is metallic with electrons as the dominant charge carriers, indicating the formation of 2DEGs at the  $\gamma$ -Al<sub>2</sub>O<sub>3</sub>/KTO interfaces. Figure 1(c) presents the temperature dependence of the sheet resistance ( $R_s$ ) for samples with different film thicknesses  $t_{\gamma\text{-Al}_2\text{O}_3} = 3, 4, 6,$  and  $8$  u.c. To evaluate the origin of the interfacial conductivity, XPS measurements are performed (see Fig. S3 in the Supplemental Material [28]). The Ta  $4f$  core-level spectrum collected from the bare KTO substrate shows only the Ta<sup>5+</sup> valence state, consistent with its insulating character. However, after depositing a  $\gamma$ -Al<sub>2</sub>O<sub>3</sub> layer with a thickness of 3 u.c., peaks associated with Ta<sup>4+</sup> and Ta<sup>2+</sup> valence states arise, indicating the generation of an electron-rich layer at the  $\gamma$ -Al<sub>2</sub>O<sub>3</sub>/KTO

heterointerface. This can be ascribed to the formation of oxygen vacancies in KTO during the deposition process of  $\gamma$ -Al<sub>2</sub>O<sub>3</sub> rather than polar-discontinuity-induced electronic reconstruction, since each layer of  $\gamma$ -Al<sub>2</sub>O<sub>3</sub> is nominally charge neutral [27].

Interfacial electrons are exclusively accumulated on the  $5d$  electronic shell of the Ta ions, residing in the  $t_{2g}$  conduction bands of KTO. As is well established, quantum confinement lifts the orbital degeneracy of the bulk band structure and leads to the hierarchic band structure of 2DEGs [19]. The  $d_{xy}$  band is lower in energy compared with the  $d_{xz}$  and/or  $d_{yz}$  bands. Therefore, at low carrier densities, all electrons are expected to populate the  $d_{xy}$  band, whereas at higher densities, after the Lifshitz transition, the Fermi energy enters the  $d_{xz}$  and/or  $d_{yz}$  bands. The Hall effect of the 2DEGs at different temperatures is further investigated (see Note 1 and Fig. S4 in the Supplemental Material [28]). Linear  $R_{xy}$ - $H$  curves are obtained for  $t_{\gamma\text{-Al}_2\text{O}_3} = 6$  and  $8$  u.c., which means that only one species of carrier exists in the system, residing in the  $d_{xy}$  band. The nonlinear Hall effect, which can be satisfactorily described by a two-band model [29], is observed for samples  $t_{\gamma\text{-Al}_2\text{O}_3} = 3$  and  $4$  u.c. This is an indication of the emergence of a second species of charge carriers occupying the  $d_{xz}$  and/or  $d_{yz}$  orbital states. In Figs. 1(d) and 1(e) we present the deduced carrier density and corresponding Hall mobility, respectively, as functions of temperature. The carrier density of the  $d_{xy}$  electrons is  $n_1 \sim 7 \times 10^{13} \text{ cm}^{-2}$  at 2 K, almost identical for different samples. The corresponding Hall mobility varies from  $\mu_1 \sim 248$  to  $404 \text{ cm}^2/\text{Vs}$ . As the thickness of the  $\gamma$ -Al<sub>2</sub>O<sub>3</sub>

layer increases from 3 to 4 u.c., the carrier density of the  $d_{xz}$  and/or  $d_{yz}$  electrons changes from  $n_2 \sim 3.3 \times 10^{12}$  to  $1.7 \times 10^{13} \text{ cm}^{-2}$  at 2 K, an increase of nearly 1 order of magnitude, but is still far less than the density of  $d_{xy}$  electrons. Such a small carrier density ( $n_2 \sim 3.3 \times 10^{12} \text{ cm}^{-2}$ ) indicates that when  $t_{\gamma\text{-Al}_2\text{O}_3} = 3$  u.c., the system undergoes a Lifshitz transition where the  $d_{xz}$  and/or  $d_{yz}$  bands start to become occupied. As for  $\mu_2$ , it takes values of 1288 to 1360  $\text{cm}^2/\text{Vs}$  at 2 K when  $t_{\gamma\text{-Al}_2\text{O}_3}$  increases from 3 to 4 u.c., which is larger than  $\mu_1$  by a factor of 3–5. This is because the  $d_{xz}$  and/or  $d_{yz}$  orbitals extend deeper in KTO, resulting in reduced scattering from interfacial defects and thus high mobility. These transport characteristics are consistent with those reported for other KTO-based heterostructures [19,20].

### B. SOT efficiency of Py/ $\gamma\text{-Al}_2\text{O}_3$ /KTO devices

The ST-FMR technique has usually been employed to evaluate the spin current induced by spin Hall effect for heavy metals [8]. Here we apply this technique to quantitatively describe the efficiency of charge-to-spin conversion at the  $\gamma\text{-Al}_2\text{O}_3$ /KTO heterointerfaces. For this purpose, Py/ $\gamma\text{-Al}_2\text{O}_3$ /KTO devices are fabricated (see Sec. II for detailed process). The optical image of the ST-FMR device and the schematic diagram of the ST-FMR experimental

setup are shown in Fig. 2(a). The left panel of Fig. 2(a) illustrates the current-induced SOT and the SOT-driven magnetization dynamics in the Py/ $\gamma\text{-Al}_2\text{O}_3$ /KTO device. A radio frequency charge current ( $I_{\text{rf}}$ ) is applied along the  $x$  axis through a ground-source-ground electrode. An in-plane magnetic field ( $H$ ) is applied at an angle  $\varphi$  with respect to the  $x$  axis. Owing to the Rashba-Edelstein effect of the 2DEG at the  $\gamma\text{-Al}_2\text{O}_3$ /KTO interface, which is induced by the spin-momentum locking determined by the spin splitting of the band structure, nonequilibrium spins accumulate and subsequently generate a spin current in the out-of-plane direction (along the  $z$  axis). The spin current is absorbed by the Py layer, producing a dampinglike torque ( $\tau_{\text{DL}}$ ), a fieldlike torque ( $\tau_{\text{FL}}$ ), or both on the magnetization of Py. In addition,  $I_{\text{rf}}$  also generates an Oersted field torque ( $\tau_{\text{Oe}}$ ). All these current-induced torques cause a precession of the Py magnetization with the same frequency as  $I_{\text{rf}}$ . Consequently, the oscillatory anisotropic magnetoresistance (AMR) together with  $I_{\text{rf}}$  result in a rectified voltage ( $V_{\text{mix}}$ ), which is detected by a lock-in amplifier and can be described by [8,30]

$$V_{\text{mix}} = V_S \frac{\Delta H^2}{\Delta H^2 + (H - H_0)^2} + V_A \frac{\Delta H(H - H_0)}{\Delta H^2 + (H - H_0)^2} + V_0, \quad (1)$$

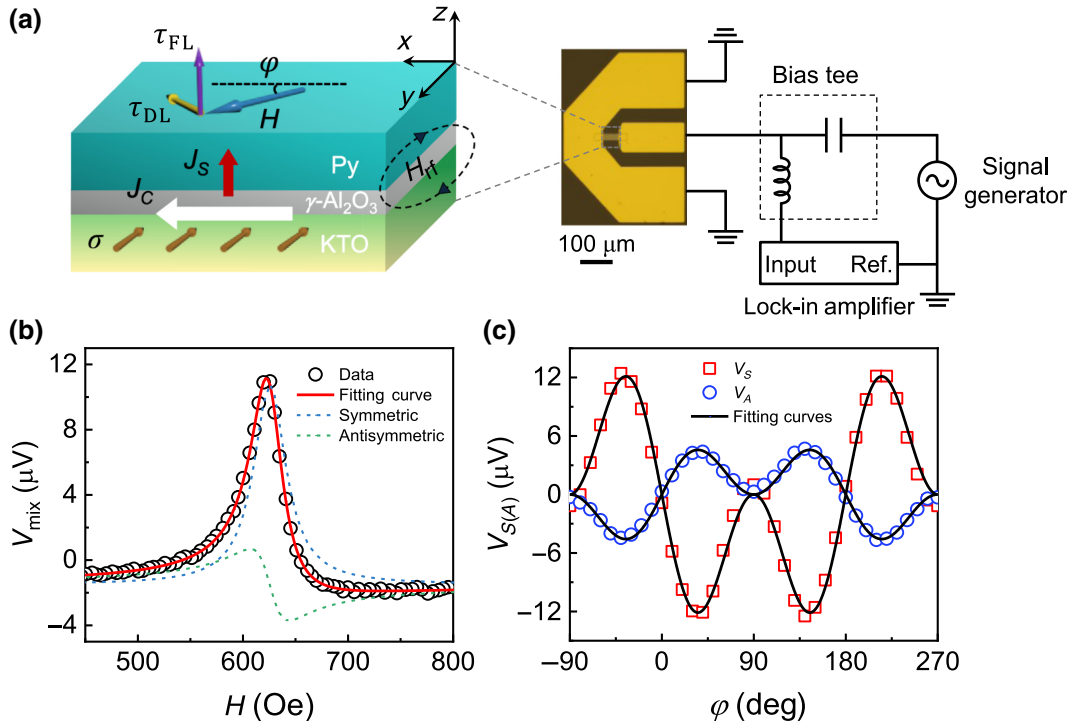


FIG. 2. (a) Schematic diagram of the structure of ST-FMR device with the SOT-induced magnetization dynamics and the ST-FMR experimental setup, where  $J_C$  is the uniform charge current density flowing through the  $\gamma\text{-Al}_2\text{O}_3$ /KTO 2DEG layer,  $J_S$  represents the spin current density injected into the Py layer, and  $\sigma$  denotes the unit vector of spin polarization. (b) Typical ST-FMR signal of Py(6 nm)/ $\gamma\text{-Al}_2\text{O}_3$ (4 u.c.)/KTO device, measured under  $f = 7$  GHz and  $\varphi = 45^\circ$  at room temperature. Symbols are experimental data and solid line is the result of curve fitting, which can be separated into symmetric (blue dashed) and antisymmetric (green dashed) components. (c) Angular dependence of  $V_S$  and  $V_A$  and the corresponding fitting curves by using the relationship of  $\sin 2\varphi \cos \varphi$ .

where  $\Delta H$  is the linewidth of the resonance peak,  $H_0$  is the resonance magnetic field, and  $V_0$  is the offset value of the measured voltage. The first term represents a symmetric Lorentzian component corresponding to the contribution of the in-plane torque ( $\tau_{\parallel} = \tau_{DL}$ ), and the second term describes an antisymmetric component corresponding to the out-of-plane torque ( $\tau_{\perp} = \tau_{FL} + \tau_{Oe}$ ).  $V_S$  and  $V_A$  are the symmetric and antisymmetric Lorentzian coefficients, respectively.

Figure 2(b) shows a representative ST-FMR spectrum of the Py(6 nm)/ $\gamma$ -Al<sub>2</sub>O<sub>3</sub>(4 u.c.)/KTO device measured by sweeping  $H$  at a fixed frequency  $f = 7$  GHz at room temperature, where  $H$  is applied at a fixed angle  $\varphi = 45^\circ$ . The ST-FMR spectrum can be quantitatively analyzed by Eq. (1). The symmetric and antisymmetric line shapes can be extracted and are shown in Fig. 2(b). Obviously, a larger symmetric signal compared with the antisymmetric component is observed. By fitting the experimental results, the parameters  $\Delta H$ ,  $H_0$ ,  $V_S$ , and  $V_A$  can be deduced. For comparison, we also measure the ST-FMR signal from the control device with a structure of Py(6 nm)/KTO under the exact same experimental conditions and obtain a negligible signal (see Fig. S5 in the Supplemental Material [28]). This result verifies that the main contribution of the current-induced SOT torque to the Py magnetization dynamics comes from the  $\gamma$ -Al<sub>2</sub>O<sub>3</sub>/KTO interface.

To get a complete result for SOT, the full angle-dependent ST-FMR measurements are carried out as the magnetic field rotates the magnetization direction of the Py layer in the sample plane at room temperature. ST-FMR spectra corresponding to different  $\varphi$  values are fitted to Eq. (1) to get the angular dependence of  $V_S$  and  $V_A$ . Notably, the amplitude corresponding to the AMR of Py has a  $\sin 2\varphi$  dependence, while the amplitude of the current-induced torque has a  $\cos\varphi$  dependence [8,30]. The product of these two contributions then yields the same angular dependence for the symmetric and antisymmetric ST-FMR components:  $V_S = S \sin 2\varphi \cos\varphi$  and  $V_A = A \sin 2\varphi \cos\varphi$ , where  $S$  and  $A$  are the averaged amplitude of  $V_S$  and  $V_A$ , respectively. Figure 2(c) shows that both  $V_S$  and  $V_A$  are well described by this angular dependence, and  $S$  and  $A$  can be determined by curve fitting. Please see Fig. S6 in the Supplemental Material [28] for the angular dependence of  $V_S$  and  $V_A$  for  $t_{\gamma\text{-Al}_2\text{O}_3} = 3, 6, \text{ and } 8$  u.c. Notably, the angular dependence of  $V_S$  and  $V_A$  are reversed, i.e., the peaks (valleys) of the  $V_S$ - $\varphi$  curve correspond to the valleys (peaks) of the  $V_A$ - $\varphi$  curve. This result indicates that the sign of  $S$  is positive while the sign of  $A$  is negative. However, both  $S$  and  $A$  of Pt are positive according to the angular dependence of  $V_S$  and  $V_A$  [31], suggesting that the Rashba effect at the  $\gamma$ -Al<sub>2</sub>O<sub>3</sub>/KTO interface is opposite in sign to that for the heavy metal Pt.

From the ratio of the symmetric and antisymmetric components, the SOT efficiency  $\xi_{\text{SOT}}$  of the Py/ $\gamma$ -Al<sub>2</sub>O<sub>3</sub>/STO device can be expressed as [32],

$$|\xi_{\text{SOT}}| = \left| \frac{S}{A} \right| \frac{e\mu_0 M_S t d}{\hbar} [1 + (4\pi M_{\text{eff}}/H_0)]^{1/2}, \quad (2)$$

where  $e$  is the electron charge,  $\hbar$  is the reduced Planck constant,  $\mu_0$  is the vacuum permeability,  $M_S$  is the saturation magnetization of the ferromagnetic Py layer,  $t$  is the thickness of the Py layer,  $d$  is the thickness of the 2DEG conducting layer (about 10 nm) [9,33], and  $4\pi M_{\text{eff}}$  is the effective magnetization of the Py layer, which can be obtained from fitting the frequency-dependent resonance field to the Kittel formula [inset in Fig. 3(a)] [32],

$$f = (\gamma/2\pi)[H_0(H_0 + 4\pi M_{\text{eff}})]^{1/2}, \quad (3)$$

where  $\gamma$  is the gyromagnetic ratio ( $\gamma = 1.76 \times 10^{11}$  rad s<sup>-1</sup> T<sup>-1</sup> for the Py film). The ST-FMR spectra of Py(6 nm)/ $\gamma$ -Al<sub>2</sub>O<sub>3</sub>( $t_{\gamma\text{-Al}_2\text{O}_3}$ )/KTO devices with  $t_{\gamma\text{-Al}_2\text{O}_3} = 3, 4, 6, \text{ and } 8$  u.c. at different resonance frequencies are recorded at room temperature, and the corresponding  $f$ - $H_0$  curves are fitted (see Figs. S7 and S8 in the Supplemental Material [28]). Based on the results of curve fitting,  $4\pi M_{\text{eff}}$  as a function of  $t_{\gamma\text{-Al}_2\text{O}_3}$  is shown in Fig. 3(a). The maximal value of  $4\pi M_{\text{eff}}$  is around 9.0 kOe, appearing at  $t_{\gamma\text{-Al}_2\text{O}_3} = 4$  u.c., and slightly decreases with the increase of  $t_{\gamma\text{-Al}_2\text{O}_3}$ . As the  $4\pi M_{\text{eff}}$  presents the contribution of interfacial anisotropy, these results indicate that the anisotropy decreases slightly with the increase of the layer thickness of  $\gamma$ -Al<sub>2</sub>O<sub>3</sub>.

To get the information on magnetic damping, the linewidth  $\Delta H$  is presented as a function of resonance frequency  $f$  when  $t_{\gamma\text{-Al}_2\text{O}_3} = 4$  u.c., as shown in the inset of Fig. 3(b). The Gilbert damping coefficient  $\alpha$  of the Py layer is estimated from the slope of the linear fitting curve, given by  $\Delta H = \Delta H_0 + (2\pi\alpha/\gamma)f$ , where  $\Delta H_0$  is the inhomogeneous line broadening factor that is usually independent of frequency [32]. Please see Fig. S9 in the Supplemental Material [28] for the fitting processes of  $\alpha$  for different samples. As shown in Fig. 3(b), with the increase of the  $\gamma$ -Al<sub>2</sub>O<sub>3</sub> layer thickness,  $\alpha$  first decreases slightly and then increases significantly, ranging from 0.0057 to 0.0132. This result matches well the result of the Py film of spin valves [10,11]. Notably, the Gilbert damping coefficient depends on disorder and electron-electron interaction [34]. The significant increase of  $\alpha$  in the case of  $t_{\gamma\text{-Al}_2\text{O}_3} = 8$  u.c. may be a consequence of increased interface roughness of the 8-u.c.- $\gamma$ -Al<sub>2</sub>O<sub>3</sub> film, which would result in stronger disorder and electron-electron scattering.

Based on the results mentioned previously, the interface SOT efficiency  $|\xi_{\text{SOT}}|$ , i.e., the efficiency for charge-to-spin conversion, can be calculated using Eq. (2) and adopting the deduced parameters. The variation of the  $|\xi_{\text{SOT}}|$  with the  $\gamma$ -Al<sub>2</sub>O<sub>3</sub> layer thickness at room temperature is presented in Fig. 3(c).  $|\xi_{\text{SOT}}|$  ranges from 0.7 to 1.1 as  $t_{\gamma\text{-Al}_2\text{O}_3}$  varies, and the highest efficiency appears when  $t_{\gamma\text{-Al}_2\text{O}_3} = 3$  u.c. Notably, the SOT efficiency detected here

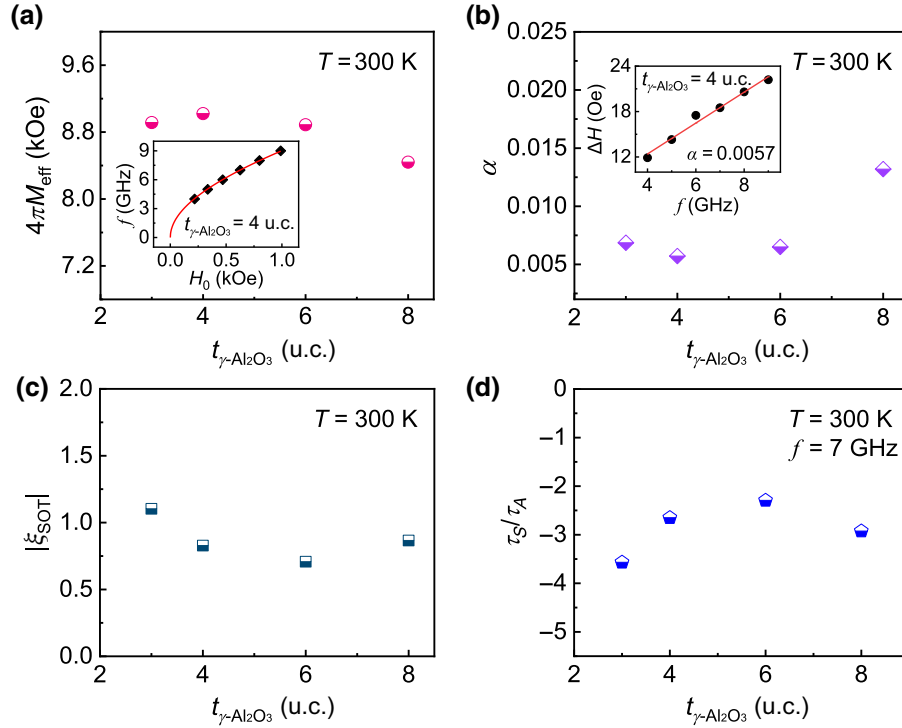


FIG. 3. (a) Effective magnetization as a function of  $\gamma$ -Al<sub>2</sub>O<sub>3</sub> layer thickness. The inset is the relationship between the resonant frequency and the resonant field for  $t_{\gamma\text{-Al}_2\text{O}_3} = 4$  u.c., and the red line is the result of fitting to the Kittel formula. (b) Dependence of Gilbert damping constant on  $\gamma$ -Al<sub>2</sub>O<sub>3</sub> layer thickness. The inset is the linewidth of the resonance peak versus the resonant frequency for  $t_{\gamma\text{-Al}_2\text{O}_3} = 4$  u.c., and the red line is the linear fitting. (c) Efficiency of charge-to-spin conversion for different  $t_{\gamma\text{-Al}_2\text{O}_3}$  at room temperature. (d) Dependence of the torque ratio  $\tau_S/\tau_A$  on  $\gamma$ -Al<sub>2</sub>O<sub>3</sub> thickness for devices at a given frequency ( $f = 7$  GHz).

is much larger than that of heavy metals (0.07 in Pt [5] and 0.3 in W [12] at 300 K). Of relevance for magnetization switching based on SOT are the relative signs and strength of the ratio between in-plane and out-of-plane torque [35,36]. The angular dependences for the in-plane torque ( $\tau_{\parallel}$ ) and the out-of-plane torque ( $\tau_{\perp}$ ) have the following forms:  $\tau_{\parallel}(\varphi) = \tau_S \cos\varphi$  and  $\tau_{\perp} = \tau_A \cos\varphi$ , where  $\tau_S$  and  $\tau_A$  are independent of  $\varphi$ , and the ratio of in-plane torque  $\tau_S$  to the out-of-plane torque  $\tau_A$  is equal to  $S/A$  [31]. Figure 3(d) shows the dependence of the torque ratio  $\tau_S/\tau_A$  on  $\gamma$ -Al<sub>2</sub>O<sub>3</sub> thickness for devices at a given frequency ( $f = 7$  GHz). As  $t_{\gamma\text{-Al}_2\text{O}_3}$  varies, the ratio  $\tau_S/\tau_A$  ranges from  $-2.3$  to  $-3.6$ . Notably, the ratio between in-plane and out-of-plane torque for the Py/ $\gamma$ -Al<sub>2</sub>O<sub>3</sub>/KTO sample has an opposite sign to that of the Py/Pt sample but is larger in absolute value than that of Py/Pt ( $\tau_S/\tau_A$  is 1.79 in magnitude for Py/Pt) [31].

### C. Fermi-level-dependent charge-to-spin conversion at low temperature

Fermi-level-dependent charge-to-spin conversion has been investigated in different materials, such as topological insulator and monolayer transition-metal dichalcogenides [37–39]. In order to reveal the relationships between SOT

efficiency and the position of the Fermi level we further perform the ST-FMR measurement at low temperature. The ST-FMR spectra of devices with different  $\gamma$ -Al<sub>2</sub>O<sub>3</sub> layer thicknesses are recorded under a fixed frequency and  $\varphi = 45^\circ$  at 5 K (see Fig. S10 in the Supplemental Material [28]). Figure 4(a) presents the relation between SOT efficiency and the Fermi energy ( $E_F$ ), obtained at 5 K for all devices.

The Fermi energy is determined by  $E_F = n_S \hbar^2 / 4\pi m_e$  with  $\hbar$  being the Planck constant and  $m_e$  being effective electron mass, and the values of  $n_S$  at 5 K in Fig. 1(d) are adopted for the calculation of  $E_F$ . Considering the difference of the effective mass for  $d_{xy}$  and  $d_{xz}$  and/or  $d_{yz}$  bands, the equation  $E_F = n_1 \hbar^2 / 4\pi m_{e1} + n_2 \hbar^2 / 4\pi m_{e2}$  is adopted when two species of carriers coexist, where  $m_{e1} = 0.31m_0$  for the  $d_{xy}$  band [40] and  $m_{e2} = 0.996m_0$  for  $d_{xz}$  and/or  $d_{yz}$  bands with  $m_0$  being free electron mass (see Note 2 in the Supplemental Material for details [28]). When there is only one species of carrier, the equation  $E_F = n_1 \hbar^2 / 4\pi m_{e1}$  is adopted.  $E_F$  ranges from about 0.549 to 0.596 eV for 5d 2DEGs at the  $\gamma$ -Al<sub>2</sub>O<sub>3</sub>/KTO heterointerfaces.  $|\xi_{\text{SOT}}|$  displays a strong dependence on the state of band filling. At low Fermi energies, only one species of carrier exists, and  $|\xi_{\text{SOT}}| = 1.4$  and 1.8 for  $E_F = 0.549$  and 0.552 eV, corresponding to  $t_{\gamma\text{-Al}_2\text{O}_3} = 8$  and 6 u.c., respectively. When  $E_F$

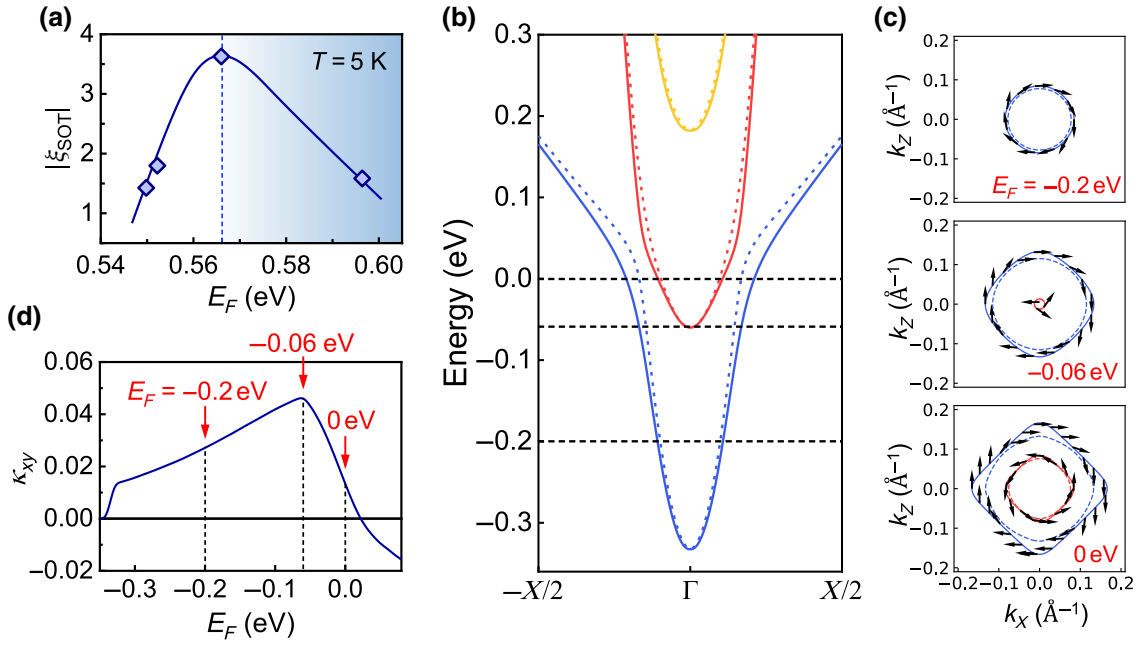


FIG. 4. (a) Charge-to-spin conversion efficiency measured at 5 K as a function of the Fermi energy, where the  $n_S$  values at 5 K in Fig. 1(d) are adopted for the calculation of  $E_F$  and the dashed line indicates the Lifshitz transition. Solid line is a guide to the eye. (b) Energy dispersion relation of the 2DEG at (001)-oriented KTO interface, calculated by a six-band tight-binding model. Dashed lines mark the positions of typical Fermi levels. (c) Fermi surfaces and spin textures at various energies corresponding to the band filling states marked in (b), arranged in energetically ascending order from top to bottom. For clarity, only clockwise (anticlockwise) spin helicity is shown for the outside (inside) Fermi contours. (d) Dependence of the theoretically calculated Edelstein tensor  $\kappa_{xy}$  on the Fermi energy.

increases to the threshold value of around 0.566 eV, the 2DEG undergoes a crossover from one to two species of charge carriers, i.e., Lifshitz transition, as marked by the dashed line in Fig. 4(a) corresponding to  $t_{\gamma-\text{Al}_2\text{O}_3} = 3$  u.c.  $|\xi_{\text{SOT}}|$  increases dramatically and the highest value of  $|\xi_{\text{SOT}}| = 3.6$  is obtained at the Lifshitz point. A further increase in  $E_F$  leads to a rapid decay of  $|\xi_{\text{SOT}}|$  to 1.6 corresponding to  $t_{\gamma-\text{Al}_2\text{O}_3} = 4$  u.c.

As mentioned previously, the spatial confinement of the 2DEG leads to hierarchic subbands and Rashba spin splitting that is enhanced by orbital hybridization [41–43]. To gain more insight into the relationship between the charge-to-spin conversion and the electronic structure of the 2DEG, we model the band structure of the (001)-oriented KTO interface using a six-band tight-binding Hamiltonian for multiband systems (see Note 3 in the Supplemental Material for details [28]). Without spin-orbit coupling, the  $t_{2g}$  bands with sixfold degeneracy at the  $\Gamma$  point are split into double and fourfold degeneracy owing to quantum confinement. Under the effect of spin-orbit interaction, the splitting of the  $d_{xy}$  and  $d_{xz}$  and/or  $d_{yz}$  orbitals occurs, lifting the degeneracy of the electronic states and resulting in six branches of dispersion relations with sizable Rashba spin splitting along the  $\Gamma$ - $X$  direction, as shown in Fig. 4(b). Representative Fermi surfaces with  $E_F = -0.2$ ,  $-0.06$ , and

$0$  eV are displayed in Fig. 4(c), corresponding to different degrees of band filling at the positions marked with dashed lines in Fig. 4(b). When the energy band filling is low ( $E_F = -0.2$  eV), a circular Fermi contour is obtained where Rashba splitting is barely visible. With the increase in band filling, when the Fermi level just crosses the bottom of the orbital with higher energy ( $E_F = -0.06$  eV), hump-shaped Fermi arcs are observed above the circular baseline across the  $k_z$  and  $k_x$  axes shown in the middle panel of Fig. 4(c). Meanwhile, a tiny Fermi ring with the opposite spin helicity appears in the center of the Fermi contour. In this case, the spin-splitting energy is as high as around 8.7 meV, which is attributed to the formation of a hump-shaped Fermi arc. As the band filling further increases to  $E_F = 0$  eV, hump Fermi arcs are more pronounced, and the inner Fermi ring expands into a larger Fermi ring [the bottom panel of Fig. 4(c)].

To explore the effect of the structural features of the Fermi surface on charge-to-spin conversion, we characterize the Rashba-Edelstein efficiency by the tensor  $\kappa$ , which relates the spin density  $\mathbf{s}$  per surface unit cell to the applied electric field  $E$  by the expression  $\mathbf{s} = \kappa E$ . As depicted in Fig. 4(d), the  $\kappa_{xy}$  calculated using the Boltzmann method [44–46] (see Note 4 in the Supplemental Material for details [28]) exhibits a strong dependence on the Fermi

energy. With the increase of Fermi energy,  $\kappa_{xy}$  grows monotonically and then reaches a peak at  $E_F = -0.06$  eV, corresponding to the Fermi level being lifted across the bottom of the  $d_{xz}$  and/or  $d_{yz}$  bands, where orbital mixing enhances Rashba splitting. The subsequent decrease in  $\kappa_{xy}$  could be ascribed to the reduced spin splitting of the  $d_{xz}$  and/or  $d_{yz}$  bands as Fermi energy grows. Lastly, for even higher energy, a sign change occurs resulting from the competing contributions from multiple bands.

Based on this theoretical analysis combined with experimental results, we can figure out the correspondence between the charge-to-spin conversion and the band filling for 2DEGs at the KTO interface. When only one species of carrier exists, mobile electrons first occupy the low-lying  $d_{xy}$  subband. In this case, the value of  $\kappa_{xy}$  is small, which is consistent with the low efficiency of charge-to-spin conversion at the low Fermi level. As the Fermi energy rises, a portion of the electrons starts to fill into the  $d_{xz}$  and/or  $d_{yz}$  orbitals, and the enhanced spin splitting results in a peak in  $\kappa_{xy}$ , and thus the highest  $|\xi_{\text{SOT}}|$  at the Lifshitz point. Subsequently,  $\kappa_{xy}$  decreases as  $E_F$  further increases, which explains the decay of  $|\xi_{\text{SOT}}|$  as the Fermi level continues to fill higher.

Recently, the direct visualization of Rashba-split bands, using angle-resolved photoemission spectroscopy, has been reported for the Al/KTO(001) surface, and the theoretical calculation, based on the tight-binding model, of the band-resolved spin and orbital Edelstein effects with respect to the Fermi level position has predicted a highly efficient spin/orbital-charge interconversion [23]. The investigation of the SOT efficiency for the Py/ $\gamma$ -Al<sub>2</sub>O<sub>3</sub>/KTaO<sub>3</sub> devices using the ST-FMR technique in our work further verifies the high efficiency of the charge-to-spin conversion in the KTO 2DEGs. Moreover, the effective modulation of SOT efficiency by changing the Fermi-level position is observed experimentally.

#### IV. CONCLUSION

In summary, we demonstrate that high-quality crystalline  $\gamma$ -Al<sub>2</sub>O<sub>3</sub> films can be epitaxially grown on (001)-oriented KTO substrates, benefiting from the excellent lattice match between the oxygen sublattices, and the transport behavior of oxide 2DEGs formed in  $\gamma$ -Al<sub>2</sub>O<sub>3</sub>/KTO spinel/perovskite heterostructures is investigated. ST-FMR measurements are performed on Py/ $\gamma$ -Al<sub>2</sub>O<sub>3</sub>/KTO devices to quantitatively determine the efficiency of charge-to-spin conversion at the  $\gamma$ -Al<sub>2</sub>O<sub>3</sub>/KTO interface originating from spin-momentum locking. The charge-to-spin conversion efficiency  $|\xi_{\text{SOT}}|$  has values of up to 3.6 for the Py(6 nm)/ $\gamma$ -Al<sub>2</sub>O<sub>3</sub>(3 u.c.)/KTO device at 5 K. The electronic structure of the 2DEG at the KTO interface calculated using the tight-binding model reveals the relationship between this efficient conversion and band filling.

As evidenced by theoretical calculation, the strong dependence of the charge-to-spin conversion on the Fermi level originates from the Rashba spin splitting of the hierarchic band structure, and the enhanced spin splitting due to orbital hybridization leads to the highest conversion efficiency when the Lifshitz transition occurs. This work provides a path to manipulate the SOT efficiency of KTO-based 2DEGs and will facilitate potential applications in spintronic devices.

#### ACKNOWLEDGMENTS

This work has been supported by the open research fund of Songshan Lake Materials Laboratory (Grant No. 2022SLABFN23), the Science Center of the National Science Foundation of China (Grant No. 52088101), the National Key Research and Development Program of China (Grants No. 2018YFA0305704, No. 2019YFA0308401, No. 2019YFA0704904, No. 2022YFA1403302, No. 2021YFA1400300, No. 2021YFB3501202, and No. 2020YFA0711502), the National Natural Science Foundation of China (Grants No. 12004022, No. 11934016, No. 51972335, No. 12104027, No. 12104029, No. 11921004, No. 11934016, and No. 12274443), the Strategic Priority Research Program (B, Grant No. XDB33030200) and the Key Research Programs (Grant No. ZDRW-CN-2021-3) of the Chinese Academy of Sciences, the Guangdong Basic and Applied Basic Research Foundation (Grants No. 2022A1515110648, No. 2023A1515010953, and No. 2022B1515120058). J.R.S. is thankful for the support of the Project for Innovative Research Team of National Natural Science Foundation of China (Grant No. 11921004).

The authors declare no competing financial interest.

- 
- [1] A. Manchon, H. C. Koo, J. Nitta, S. M. Frolov, and R. A. Duine, New perspectives for Rashba spin-orbit coupling, *Nat. Mater.* **14**, 871 (2015).
  - [2] A. Ohtomo and H. Y. Hwang, A high-mobility electron gas at the LaAlO<sub>3</sub>/SrTiO<sub>3</sub> heterointerface, *Nature* **427**, 423 (2004).
  - [3] E. Lesne, Y. Fu, S. Oyarzun, J. C. Rojas-Sanchez, D. C. Vaz, H. Naganuma, G. Sicoli, J. P. Attane, M. Jamet, E. Jacquet, J. M. George, A. Barthelemy, H. Jaffres, A. Fert, M. Bibes, and L. Vila, Highly efficient and tunable spin-to-charge conversion through Rashba coupling at oxide interfaces, *Nat. Mater.* **15**, 1261 (2016).
  - [4] V. M. Edelstein, Spin polarization of conduction electrons induced by electric current in two-dimensional asymmetric electron systems, *Solid State Commun.* **73**, 233 (1990).
  - [5] I. Mihai Miron, K. Garello, G. Gaudin, P. J. Zermatten, M. V. Costache, S. Auffret, S. Bandiera, B. Rodmacq, A. Schuhl, and P. Gambardella, Perpendicular switching of a single ferromagnetic layer induced by in-plane current injection, *Nature* **476**, 189 (2011).



- [6] L. Liu, C. F. Pai, Y. Li, H. W. Tseng, D. C. Ralph, and R. A. Buhrman, Spin-torque switching with the giant spin Hall effect of tantalum, *Science* **336**, 555 (2012).
- [7] A. Brataas and K. M. D. Hals, Spin-orbit torques in action, *Nat. Nanotechnol.* **9**, 86 (2014).
- [8] L. Q. Liu, T. Moriyama, D. C. Ralph, and R. A. Buhrman, Spin-Torque Ferromagnetic Resonance Induced by the Spin Hall Effect, *Phys. Rev. Lett.* **106**, 036601 (2011).
- [9] Y. Wang, R. Ramaswamy, M. Motapothula, K. Narayana-pillai, D. Zhu, J. Yu, T. Venkatesan, and H. Yang, Room-temperature giant charge-to-spin conversion at the SrTiO<sub>3</sub>-LaAlO<sub>3</sub> oxide interface, *Nano Lett.* **17**, 7659 (2017).
- [10] J. Zhang, J. Zhang, X. Chi, R. Hao, W. Chen, H. Yang, D. Zhu, Q. Zhang, W. Zhao, H. Zhang, and J. R. Sun, Giant efficiency for charge-to-spin conversion via the electron gas at the LaTiO<sub>3+δ</sub>/SrTiO<sub>3</sub> interface, *Phys. Rev. B* **105**, 195110 (2022).
- [11] H. W. Yang, B. Y. Zhang, X. Y. Zhang, X. Yan, W. L. Cai, Y. L. Zhao, J. R. Sun, K. L. Wang, D. P. Zhu, and W. S. Zhao, Giant Charge-to-Spin Conversion Efficiency in SrTiO<sub>3</sub>-Based Electron Gas Interface, *Phys. Rev. Appl.* **12**, 034004 (2019).
- [12] X. Qiu, K. Narayanapillai, Y. Wu, P. Deorani, D. H. Yang, W. S. Noh, J. H. Park, K. J. Lee, H. W. Lee, and H. Yang, Spin-orbit-torque engineering via oxygen manipulation, *Nat. Nanotechnol.* **10**, 333 (2015).
- [13] X. Tao, Q. Liu, B. Miao, R. Yu, Z. Feng, L. Sun, B. You, J. Du, K. Chen, S. Zhang, L. Zhang, Z. Yuan, D. Wu, and H. Ding, Self-consistent determination of spin Hall angle and spin diffusion length in Pt and Pd: The role of the interface spin loss, *Sci. Adv.* **4**, eaat1670 (2018).
- [14] P. Noel, F. Trier, L. M. Vicente Arche, J. Brehin, D. C. Vaz, V. Garcia, S. Fusil, A. Barthelemy, L. Vila, M. Bibes, and J. P. Attane, Non-volatile electric control of spin-charge conversion in a SrTiO<sub>3</sub> Rashba system, *Nature* **580**, 483 (2020).
- [15] D. C. Vaz, *et al.*, Mapping spin-charge conversion to the band structure in a topological oxide two-dimensional electron gas, *Nat. Mater.* **18**, 1187 (2019).
- [16] D. Choe, M. J. Jin, S. I. Kim, H. J. Choi, J. Jo, I. Oh, J. Park, H. Jin, H. C. Koo, B. C. Min, S. Hong, H. W. Lee, S. H. Baek, and J. W. Yoo, Gate-tunable giant nonreciprocal charge transport in noncentrosymmetric oxide interfaces, *Nat. Commun.* **10**, 4510 (2019).
- [17] K. Zou, S. Ismail-Beigi, K. Kisslinger, X. Shen, D. Su, F. J. Walker, and C. H. Ahn, LaTiO<sub>3</sub>/KTaO<sub>3</sub> interfaces: A new two-dimensional electron gas system, *APL Mater.* **3**, 036104 (2015).
- [18] H. Zhang, H. R. Zhang, X. Yan, X. J. Zhang, Q. H. Zhang, J. Zhang, F. R. Han, L. Gu, B. G. Liu, Y. S. Chen, B. G. Shen, and J. R. Sun, Highly mobile two-dimensional electron gases with a strong gating effect at the amorphous LaAlO<sub>3</sub>/KTaO<sub>3</sub> interface, *ACS Appl. Mater. Interfaces* **9**, 36456 (2017).
- [19] H. Zhang, X. Yan, X. J. Zhang, S. Wang, C. M. Xiong, H. R. Zhang, S. J. Qi, J. N. Zhang, F. R. Han, N. Wu, B. G. Liu, Y. S. Chen, B. G. Shen, and J. R. Sun, Unusual electric and optical tuning of KTaO<sub>3</sub>-based two-dimensional electron gases with 5d orbitals, *ACS Nano* **13**, 609 (2019).
- [20] H. Zhang, X. Yan, J. Zhang, J. E. Zhang, F. R. Han, H. L. Huang, S. J. Qi, W. X. Shi, B. G. Shen, and J. R. Sun, The effect of fabrication conditions on 2DEGs transport characteristics at amorphous-LaAlO<sub>3</sub>/KTaO<sub>3</sub> interfaces, *Mater. Res. Express.* **6**, 086448 (2019).
- [21] H. Uwe, K. Oka, H. Unoki, and T. Sakudo, Raman scattering from conduction electron in KTaO<sub>3</sub>, *J. Phys. Soc. Jpn.* **49**, 577 (1980).
- [22] H. Uwe, T. Sakudo, and H. Yamaguchi, Interband electronic Raman scattering in SrTiO<sub>3</sub>, *Jpn. J. Appl. Phys.* **24**, 519 (1985).
- [23] S. Varotto, A. Johansson, B. Gobel, L. M. Vicente-Arche, S. Mallik, J. Brehin, R. Salazar, F. Bertran, P. Le Fevre, N. Bergeal, J. Rault, I. Mertig, and M. Bibes, Direct visualization of Rashba-split bands and spin/orbital-charge interconversion at KTaO<sub>3</sub> interfaces, *Nat. Commun.* **13**, 6165 (2022).
- [24] H. R. Zhang, Y. Ma, H. Zhang, X. B. Chen, S. H. Wang, G. Li, Y. Yun, X. Yan, Y. S. Chen, F. X. Hu, J. W. Cai, B. G. Shen, W. Han, and J. R. Sun, Thermal spin injection and inverse Edelstein effect of the two-dimensional electron gas at EuO-KTaO<sub>3</sub> interfaces, *Nano Lett.* **19**, 1605 (2019).
- [25] L. M. Vicente-Arche, *et al.*, Spin-charge interconversion in KTaO<sub>3</sub> 2D electron gases, *Adv. Mater.* **33**, 2102102 (2021).
- [26] J. M. McHale, A. Auroux, A. J. Perrotta, and A. Navrotsky, Surface energies and thermodynamic phase stability in nanocrystalline aluminas, *Science* **277**, 788 (1997).
- [27] Y. Z. Chen, N. Bovet, F. Trier, D. V. Christensen, F. M. Qu, N. H. Andersen, T. Kasama, W. Zhang, R. Giraud, J. Dufouleur, T. S. Jespersen, J. R. Sun, A. Smith, J. Nygard, L. Lu, B. Buechner, B. G. Shen, S. Linderoth, and N. Pryds, A high-mobility two-dimensional electron gas at the spinel/perovskite interface of gamma-Al<sub>2</sub>O<sub>3</sub>/SrTiO<sub>3</sub>, *Nat. Commun.* **4**, 1371 (2013).
- [28] See Supplemental Material at <http://link.aps.org/supplemental/10.1103/PhysRevApplied.19.034045> for more detailed information about the two-band model, calculation of Fermi energy, the tight-binding three-band model and Edelstein efficiency for theoretical calculation, RHEED intensity during deposition, AFM image, x-ray photoelectron spectroscopy, Hall effect at different temperatures, ST-FMR signal for Py(6 nm)/KTO compared with Py(6 nm)/γ-Al<sub>2</sub>O<sub>3</sub>(4 uc)/KTO sample, angular dependence of  $V_S$  and  $V_A$  for additional devices, ST-FMR spectra with different resonance frequencies, additional fitting processes to get the Gilbert damping coefficient and the effective magnetization for additional devices, and ST-FMR results at low temperature.
- [29] F. Gunkel, C. Bell, H. Inoue, B. Kim, A. G. Swartz, T. A. Merz, Y. Hikita, S. Harashima, H. K. Sato, M. Minohara, S. Hoffmann-Eifert, R. Dittmann, and H. Y. Hwang, Defect Control of Conventional and Anomalous Electron Transport at Complex Oxide Interfaces, *Phys. Rev. X* **6**, 031035 (2016).
- [30] A. R. Mellnik, J. S. Lee, A. Richardella, J. L. Grab, P. J. Mintun, M. H. Fischer, A. Vaezi, A. Manchon, E. A. Kim, N. Samarth, and D. C. Ralph, Spin-transfer torque generated by a topological insulator, *Nature* **511**, 449 (2014).
- [31] D. MacNeill, G. M. Stiehl, M. H. D. Guimaraes, R. A. Buhrman, J. Park, and D. C. Ralph, Control of spin-orbit

- torques through crystal symmetry in WTe<sub>2</sub>/ferromagnet bilayers, *Nat. Phys.* **13**, 300 (2017).
- [32] T. X. Nan, S. Emori, C. T. Boone, X. J. Wang, T. M. Oxholm, J. G. Jones, B. M. Howe, G. J. Brown, and N. X. Sun, Comparison of spin-orbit torques and spin pumping across NiFe/Pt and NiFe/Cu/Pt interfaces, *Phys. Rev. B* **91**, 214416 (2015).
- [33] O. Copie, V. Garcia, C. Bodefeld, C. Carretero, M. Bibes, G. Herranz, E. Jacquet, J. L. Maurice, B. Vinter, S. Fusil, K. Bouzehouane, H. Jaffres, and A. Barthelemy, Towards Two-Dimensional Metallic Behavior at LaAlO<sub>3</sub>/SrTiO<sub>3</sub> Interfaces, *Phys. Rev. Lett.* **102**, 216804 (2009).
- [34] E. M. Hankiewicz, G. Vignale, and Y. Tserkovnyak, Inhomogeneous Gilbert damping from impurities and electron-electron interactions, *Phys. Rev. B* **78**, 020404(R) (2008).
- [35] T. Taniguchi, S. Mitani, and M. Hayashi, Critical current destabilizing perpendicular magnetization by the spin Hall effect, *Phys. Rev. B* **92**, 024428 (2015).
- [36] D. J. P. de Sousa, P. M. Haney, J. Wang, and T. Low, Field-Free-Switching State Diagram of Perpendicular Magnetization Subjected to Conventional and Unconventional Spin-Orbit Torques, *Phys. Rev. Appl.* **18**, 054020 (2022).
- [37] Q. Lu, P. Li, Z. X. Guo, G. H. Dong, B. Peng, X. Zha, T. Min, Z. Y. Zhou, and M. Liu, Giant tunable spin Hall angle in sputtered Bi<sub>2</sub>Se<sub>3</sub> controlled by an electric field, *Nat. Commun.* **13**, 1650 (2022).
- [38] H. Wu, P. Zhang, P. Deng, Q. Q. Lan, Q. J. Pan, S. A. Razavi, X. Y. Che, L. Huang, B. Q. Dai, K. Wong, X. F. Han, and K. L. Wang, Room-Temperature Spin-Orbit Torque from Topological Surface States, *Phys. Rev. Lett.* **123**, 207205 (2019).
- [39] D. J. P. de Sousa, M. J. Sammon, R. Kim, H. Li, I. A. Young, and T. Low, Spin torque generated by valley Hall effect in WSe<sub>2</sub>, *Phys. Rev. B* **106**, 184412 (2022).
- [40] P. D. C. King, R. H. He, T. Eknapakul, P. Buaphet, S. K. Mo, Y. Kaneko, S. Harashima, Y. Hikita, M. S. Bahramy, C. Bell, Z. Hussain, Y. Tokura, Z. X. Shen, H. Y. Hwang, F. Baumberger, and W. Meevasana, Subband Structure of a Two-Dimensional Electron Gas Formed at the Polar Surface of the Strong Spin-Orbit Perovskite KTaO<sub>3</sub>, *Phys. Rev. Lett.* **108**, 117602 (2012).
- [41] Z. Zhong, A. Toth, and K. Held, Theory of spin-orbit coupling at LaAlO<sub>3</sub>/SrTiO<sub>3</sub> interfaces and SrTiO<sub>3</sub> surfaces, *Phys. Rev. B* **87**, 161102(R) (2013).
- [42] P. D. C. King, S. M. Walker, A. Tamai, A. de la Torre, T. Eknapakul, P. Buaphet, S. K. Mo, W. Meevasana, M. S. Bahramy, and F. Baumberger, Quasiparticle dynamics and spin-orbital texture of the SrTiO<sub>3</sub> two-dimensional electron gas, *Nat. Commun.* **5**, 3414 (2014).
- [43] G. Khalsa and A. H. MacDonald, Theory of the SrTiO<sub>3</sub> surface state two-dimensional electron gas, *Phys. Rev. B* **86**, 125121 (2012).
- [44] I. Mertig, Transport properties of dilute alloys, *Rep. Prog. Phys.* **62**, 237 (1999).
- [45] A. Johansson, J. Henk, and I. Mertig, Theoretical aspects of the Edelstein effect for anisotropic two-dimensional electron gas and topological insulators, *Phys. Rev. B* **93**, 195440 (2016).
- [46] J. E. Zhang, H. Zhang, X. B. Chen, J. Zhang, S. J. Qi, F. R. Han, Y. S. Chen, W. S. Zhao, F. X. Hu, B. G. Shen, and J. R. Sun, Anisotropic bilinear magnetoresistance in (110) SrTiO<sub>3</sub>-based two-dimensional electron gas, *Phys. Rev. B* **104**, 045114 (2021).